Monthly Notices of the ROYAL ASTRONOMICAL SOCIETY

MNRAS **539,** 82–94 (2025) https://doi.org/10.1093/mnras/staf476
Advance Access publication 2025 March 24

Gaseous methanol in cold environments: is thermal desorption from low binding energy sites the explanation?

Vittorio Bariosco [1,2★] Lorenzo Tinacci,[3] Stefano Pantaleone [1] Cecilia Ceccarelli [3★] Albert Rimola [2] and Piero Ugliengo [1★]

[1]*Dipartimento di Chimica, Università degli Studi di Torino, via P. Giuria 7, I-10125 Torino, Italy*
[2]*Departament de Química, Universitat Autònoma de Barcelona, E-08193 Bellaterra, Catalonia, Spain*
[3]*CNRS, IPAG, Univ. Grenoble Alpes, F-38000 Grenoble, France*

Accepted 2025 March 20. Received 2025 March 12; in original form 2025 January 27

ABSTRACT

Methanol (CH_3OH) is the simplest and most abundant interstellar complex organic molecule (iCOM) observed in warm and cold environments. It is thought to be formed on the surfaces of dust grains and released into the gas-phase by thermal desorption of the ices in the warm regions where the dust temperature is high ($\geq$100 K). However, the presence of gaseous methanol in cold environments represented a challenge since its detection, e.g. in cold molecular clouds, prestellar cores, and protoplanetary discs. The reason is that thermal desorption was thought to be completely inefficient in these conditions. In this work, we show that this is not the case. Specifically, we present new calculations of the binding energy (BE) distribution on an iced grain composed of 200 water molecules. On this grain we obtained 223 unique sites with different BE. We found that the methanol BE distribution is well reproduced by a Gaussian function with a mean of 35.5 kJ mol^{-1} (4255 K) and a standard deviation of 13.0 kJ mol^{-1} (1558 K). To facilitate the incorporation of our calculations into astrochemical models, we provide a table with the fraction of sites as a function of the BE and the corresponding prefactors. Comparison with published experimental BE values suggests that they are dominated by the larger BE sites. Finally, and most importantly, our calculations show that 2 per cent of the BEs are around 10 kJ mol^{-1} (1240 K), implying that thermal desorption from these sites may explain the presence of gaseous methanol in cold environments.

Key words: astrochemistry – molecular data – protoplanetary discs – ISM: clouds – ISM: molecules.

1 INTRODUCTION

Methanol (CH_3OH) is one of the simplest and most abundant of the so-called interstellar complex organic molecules (iCOMs), which are species containing at least six atoms of which at least one is a carbon (Herbst & van Dishoeck 2009; Ceccarelli et al. 2017). Actually, CH_3OH is considered the mother of numerous other iCOMs, as explained in detail below, and, hence, of primary importance in the development of interstellar molecular complexity.

Methanol is ubiquitous in the molecular interstellar medium (ISM), observed in both the gaseous and solid phases. It was first detected more than 50 yrs ago towards the bright galactic center sources Sgr A and B2 (Ball et al. 1970), via the rotational lines in the millimeter wavelengths. Since then, gaseous methanol has been observed towards cold molecular clouds (e.g. Friberg et al. 1988; Spezzano et al. 2022), molecular filaments (Chahine et al. 2022b), prestellar cores (e.g. Vastel et al. 2014; Scibelli & Shirley 2020; Punanova et al. 2022), hot cores (e.g. Cummins, Linke & Thaddeus 1986; Blake et al. 1987; Bisschop et al. 2007), hot corinos (e.g. Cazaux et al. 2003; Maret et al. 2005; Taquet et al. 2015), protostellar molecular shocks (e.g. Bachiller et al. 1995; Codella et al. 2020; Chahine et al. 2024), and protoplanetary discs (e.g. Walsh et al. 2016; Lee et al. 2022; Yamato et al. 2024). In addition, observations in the infrared (IR) region have revealed that methanol is one of the major components of the ices that envelope the interstellar dust-refractory cores (e.g. Grim et al. 1991; Bottinelli et al. 2010; McClure et al. 2023). Finally, methanol has been also detected in external galaxies (e.g. Martín, Martín-Pintado & Mauersberger 2006; Harada et al. 2019) and Solar system comets (e.g. Bockelee-Morvan et al. 1991; Faggi et al. 2023; Lippi et al. 2024).

The abundance of gaseous methanol in the different environments varies by orders of magnitude, likely reflecting the mechanism of its formation, destruction and release into the gas-phase. In cold ($\leq$100 K) environments, e.g. molecular clouds, prestellar cores, cold envelopes of low-mass protostars and outer protoplanetary disc, gaseous methanol is observed with an abundance relative to H_2 less than about 10^{-8} (e.g. Friberg et al. 1988; Smith, Herbst & Chang 2004; Maret et al. 2005; Öberg et al. 2010; Vastel et al. 2014; Walsh et al. 2016; Punanova et al. 2022). In warm ($\geq$100 K) environments, e.g. hot cores/corinos and protostellar molecular shocks, gaseous methanol has a much larger abundance, up to 10^{-6} (e.g. Menten et al. 1988; Van der Tak, van Dishoeck & Caselli 2000; Taquet et al. 2015; Codella et al. 2020; Chen et al. 2023). Finally, the abundance

★ E-mail: vittorio.bariosco@unito.it (VB); cecilia.ceccarelli@univ-grenoble-alpes.fr (CC); piero.ugliengo@unito.it (PU)

of methanol in the solid state is approximately 10–20 per cent of that of frozen water, namely approximately $1–2\times10^{-5}$ (Boogert, Gerakines & Whittet 2015; McClure et al. 2023; Chen et al. 2024) assuming a water abundance of 10^{-4}.

In the gas-phase, methanol is mainly formed by the radiative association of H_2O and CH_3^+ leading to protonated methanol that, finally, produces methanol via dissociative recombination. However, this route does not seem to be efficient enough to explain the observations (e.g. Garrod et al. 2006), as laboratory experiments of the latter reaction (Geppert et al. 2006) have measured a branching fraction of the methanol product $\leq$4 per cent. Alternatively, protonated methanol could pass the proton to ammonia and, in this case, the efficiency is higher depending on the gaseous ammonia abundance (Rodgers & Charnley 2001; Taquet, Wirström & Charnley 2016). In addition, the direct reaction of gaseous CH_3^+ with frozen water molecules can also lead to the formation of methanol on the surfaces of cold grains (Woon 2011; Nakai et al. 2023).

On the other hand, it is well know that methanol is efficiently formed in both refractory and icy surfaces. Several laboratory experiments showed that methanol can be efficiently formed in both CO-rich (e.g. Hidaka et al. 2004; Fuchs et al. 2009; Bergner, Öberg & Rajappan 2017), mixed H_2O/CO (e.g. Watanabe & Kouchi 2002; Santos et al. 2022; Tsuge & Watanabe 2023) and H_2O-rich ice phases (e.g. Qasim et al. 2018; Potapov et al. 2021). Furthermore, theoretical computations demonstrated the catalytic effect of both icy and refractory surfaces in the formation process of methanol (e.g. Rimola et al. 2014; Song & Kästner 2017; Pareras et al. 2023; Martinez-Bachs et al. 2024a).

Although many details are not completely known and the final results strongly depend on several assumed parameters, astrochemical models predict that the abundance of methanol on grain surfaces is a substantial fraction (actually up to 100 per cent) of that of frozen CO (e.g. Taquet, Ceccarelli & Kahane 2012; Aikawa et al. 2020; Kalvāns 2021) Once formed on the grain surfaces, a mechanism must be in place to release the methanol into the gas phase, where it is widely observed (see above). This could be due to thermal or non-thermal desorption, depending on the specific physical conditions prevailing in the local environment. For example, in hot cores/corinos, frozen methanol is believed to be released into the gas-phase by thermal desorption of the grain icy mantles (e.g. Charnley et al. 1995; Maret et al. 2005; Bisschop et al. 2007; Taquet et al. 2015; Yang et al. 2021; Vastel et al. 2022; Chahine et al. 2022a). In colder environments ($\leq$100 K), however, thermal desorption cannot occur and several non-thermal mechanisms have been invoked in the literature, again depending on the physical conditions of the environment. For example, in shocks produced by protostellar jets and molecular outflows, a fraction of the grain icy mantles are liberated into the gas phase because of the sputtering and shattering of the grains (e.g. Pineau des Forets et al. 1993; Caselli, Hartquist & Havnes 1997; Schilke et al. 1997; May et al. 2000; Gusdorf et al. 2008; Codella et al. 2020). In the so-called Photo-Dissociated Regions, in principle incidence of UV photons might photo-desorb the frozen methanol into the gas phase, but laboratory experiments show that the process would mostly destroy methanol (Bertin et al. 2016), rendering the mechanism inefficient. In cold ($\sim$10 K) objects, cosmic rays have been also suggested to liberate frozen methanol into the gas-phase, based on laboratory experiments (Dartois et al. 2020) and theoretical considerations (Shingledecker et al. 2020), but the process is not efficient enough to reproduce the observed methanol abundances (e.g. Wakelam et al. 2021). Finally, given the failure of the other mechanisms in reproducing the observations, the so-called chemical desorption (CD) is often assumed in astrochemical models to explain the gaseous methanol in these cold environments. The idea is that part of the energy liberated by reactions occurring on the grain surfaces is acquired by the newly formed molecule and it is enough to break the interactions with the surface (e.g. Duley & Williams 1993; Willacy, Rawlings & Williams 1994; Garrod, Wakelam & Herbst 2007). In the specific case of methanol, laboratory experiments have been unable to detect gaseous methanol when formed by the successive hydrogenation of frozen CO on the surfaces, providing an upper limit on the CD efficiency $\leq$7 per cent (Minissale et al. 2016; Chuang et al. 2018; Ligterink et al. 2018). Recent *ab initio* molecular dynamics (AIMD) simulations on the formation of H_2, HCO, and NH_3 have shown that 50–90 per cent of the formation energy is rapidly transferred to the ice phonons, depending on the reaction, while the rest remains trapped in the energy levels of the adsorbed molecule, which excites its vibrational energy (Pantaleone et al. 2020, 2021; Ferrero et al. 2023). In summary, the abundance of gaseous methanol depends not only on its formation and destruction routes but also on the mechanisms that inject the frozen methanol into the gas-phase in the different environments. The very basic parameter that governs the latter is the binding energy (BE) on the water ice surfaces (Minissale et al. 2022; Ceccarelli et al. 2023). Two distinct approaches can be used to evaluate the BE: laboratory experiments, usually through temperature programmed desorption (TPD) experiments (e.g. Minissale et al. 2022; Ligterink & Minissale 2023), and theoretical calculations (e.g. Ferrero et al. 2020; Bovolenta et al. 2022; Perrero et al. 2022; Tinacci et al. 2022; Martínez-Bachs et al. 2024b). Recently, in both fields, it has been recognized that the adsorption of a species on an amorphous water surface (AWS) cannot be explained by a single BE value but rather by a distribution of BEs (Chaabouni et al. 2018; Bovolenta et al. 2022; Ferrero et al. 2022; Germain et al. 2022; Tinacci et al. 2022; Bariosco et al. 2024; Kakkenpara Suresh et al. 2024; Perrero et al. 2024).

This has a great impact on our understanding of when and where frozen species thermally and/or non-thermally sublimate. Taking the example of water interacting with itself (i.e. a water molecule adsorbed on AWS), Tinacci et al. (2023) showed that the water snowline in protoplanetary discs is extremely different if calculated assuming a single BE or a distribution. Using the same approach, in this work we present the methanol BE distribution on AWS and its implications in astrochemical models and laboratory experiments. Our goal is to understand whether the fact that methanol, as any other frozen species on water ice mantles, has a distribution of BE can help solving the puzzle of gaseous methanol in cold environments. To this end, we employ state of the art theoretical calculations based on quantum mechanical (QM) methods, adopting a similar strategy as used in previous studies from our group (Germain et al. 2022; Tinacci et al. 2022, 2023; Bariosco et al. 2024).

The article is organized as follows. In Section 2, we describe the used methodology; in Section 3, we report the results of our calculations; in Section 4, we discuss the comparison of our derived BE distribution with previous estimated of methanol BE and the astrochemical implications. Section 5 summarizes the major results and implication of this study.

2 METHODOLOGY

In order to compute the BE distribution, the methodology adopted in this article is based on previous works by our group (Germain et al. 2022; Tinacci et al. 2023; Bariosco et al. 2024).

The BE (positive for a bounded system) is defined as the opposite of the interaction energy (ΔE):

$$\mathrm{BE} = -\Delta E = E_{\mathrm{ads}}^{\mathrm{iso}} + E_{\mathrm{grn}}^{\mathrm{iso}} - E_{\mathrm{c}} \ , \tag{1}$$

where (E_{c}) is the energy of the (grain + adsorbate) complex, while ($E_{\mathrm{ads}}^{\mathrm{iso}}$) and ($E_{\mathrm{grn}}^{\mathrm{iso}}$) the energies of the isolated adsorbate and grain, respectively. The BE can be decomposed in two terms: (*i*) the pure electronic interaction ($\mathrm{BE_e}$) corrected, if needed, for the Basis Set Superposition Error (BSSE), and (*ii*) the geometry deformation energy (δE_{def}) contribution. When each electronic energy is corrected for the zero-point energy (ZPE) term derived from the harmonic frequency calculation, the BE can be corrected for these contributions giving the Binding Enthalpy at 0 K, as follows:

$$\mathrm{BE} = \underbrace{\mathrm{BE_e} - \delta E_{\mathrm{def}}}_{\mathrm{BE}^*} - \Delta\mathrm{ZPE} \ . \tag{2}$$

In the following, we refer to the BE corrected for ZPE as BE, while the same value not corrected is labelled as BE^*. The ΔZPE is computed as:

$$\Delta\mathrm{ZPE} = \mathrm{ZPE_c} - \mathrm{ZPE}_{\mathrm{ads}}^{\mathrm{iso}} - \mathrm{ZPE}_{\mathrm{gra}}^{\mathrm{iso}}. \tag{3}$$

The mathematical details are reported in the appendix B.

2.1 Computational methods

The grain model and the initial grain-adsorbate structures were first optimized at semi-empirical (SQM) GFN2-XTB level (Grimme, Bannwarth & Shushkov 2017; Bannwarth, Ehlert & Grimme 2019) to get a preliminary set of BEs. Each preliminary structure was refined using the ONIOM method (Mayhall, Raghavachari & Hratchian 2010) (QM:SQM) implemented in the ORCA programme (v.5.0.3) (Neese 2022). Within the ONIOM method, the structure is divided into two fictitious subsystems: (i) the Real Zone, which is the whole system treated at lower level of theory (SQM); (ii) the Model Zone, which is a smaller part of the structure ensuring that there are sufficient water molecules present to account for the significant local interactions of the adsorbate, treated with a higher level of theory (QM). The final ONIOM energy for each structure is obtained as:

$$E(\mathrm{ONIOM}) = E_{\mathrm{Real}}(\mathrm{SQM}) - E_{\mathrm{Model}}(\mathrm{SQM}) + E_{\mathrm{Model}}(\mathrm{QM}). \tag{4}$$

The B97-3 (Brandenburg et al. 2018) was selected as the high QM level method for the Model zone in order to compute geometries and harmonic frequencies, while GFN2-XTB was set as low SQM level method. The atoms outside the Model region are kept fixed and the Model zone is embedded electrostatically (default setting). Tight convergence criteria were set for both the self-consistent field (SCF) and geometry optimizer, while for the integral evaluation the grid was set to the highest density (keywords *!tightscf*, *!tightopt*, and *!defgrid3* in the ORCA programme). In the few cases in which imaginary frequencies were found, the geometry was restarted using a tighter convergence criterion on the optimization (i.e.*!verytightopt*), mostly leading to the minima. After the optimization procedure, energies were refined applying the DLPNO-CCSD(T) (Guo et al. 2018) as QM method in the ONIOM scheme, while keeping GFN2 as SQM. Along with this, the aug-cc-pVTZ was selected as primary basis set (Kendall, Dunning Jr & Harrison 1992; Woon & Dunning 1993), while the aug-cc-pVTZ/C (Weigend, Köhn & Hättig 2002) was used as auxiliary basis set for the resolution of the identity approximation. DLPNO-CCSD(T) calculations were performed with a tight-PNO set up and using the default settings on the SCF convergence. Finally, the energies of the complex (E_{c}(DLPNO-CCSD(T)) were corrected for the BSSE applying the Counterpoise method (Boys & Bernardi 1970).

2.2 Water-ice grain model and strategy to compute BEs

The initial BE computation is performed in the same way as in our previous work (Germain et al. 2022). A cluster of 200 water molecules is used as a model for the interstellar icy grains (see 200-water grain model at https://aurelegermain.github.io/JSmol_grain/). Using the ACO-FROST code (Germain et al. 2022), we generate a spherical grid of 162 points evenly spaced around the cluster. A methanol molecule is docked at each point, assuming three different initial orientations to maximize the variety of adsorption poses. This results in a total of 486 starting adsorption positions. These positions are then projected to a distance of 2.5–3.0 Å from the grain surface.

The strategy to compute the methanol BE distribution on the 200 water cluster model consists of five steps, as follows:

(i) We fix the geometry of the grain model and run a GFN2 geometry optimization of the adsorbed methanol molecule, for each starting position (486 BE sites).

(ii) Starting from point (*i*), all water molecules within a 5 Å region around the relaxed adsorbed methanol are allowed to relax at GFN2 level (486 BE sites).

(iii) On the resulting optimized structure of point (*ii*), a further check is carried out to ensure the 5 Å region has not changed its number of water molecules due to the geometry relaxation. In case this happened, the (*ii*)-(*iii*) points are repeated until no compositional changes in the 5 Å region is detected (486 BE sites).

(iv) Due to the high number of points used to sample the surface, several equivalent minima are found at the end of these initial three steps. To avoid this bias, we adopted a pruning procedure (described in Section 2.3), which identified 263 redundant sites.

(v) On the final structures of point (*iv*) (223 BE sites), the two-layer ONIOM(QM:SQM) model chemistry is carried out. The Model zone (corresponding to the 5 Å region) is treated with a high-level QM method, while both the Model zone and the whole cluster (the Real system) are treated at GFN2 level. The resulting energies are then combined in a subtractive way as defined by the ONIOM method [see equation (4)].

(vi) During the ONIOM geometry optimization all atoms outside the Model zone are kept fixed; electrostatical embedding of the Model zone are taken into account by activating the corresponding keywords in the computer programme. In the frequency calculations (within the harmonic approximation), only the normal modes related to the nuclei inside the Model zone are taken into account, keeping fixed all the other nuclei. As for steps (*ii*) and (*iii*) we ensure that the Model zone remains with the same number of water molecules during the geometry optimization. The isolated grain surface ($E_{\mathrm{grn}}^{\mathrm{iso}}$) is computed following our previous approach (called '*TPD*') which resembles closely the physics of the experimental TPD process (Tinacci et al. 2023), relaxing the QM system after withdrawing the adsorbed methanol molecule.

2.3 Procedure to obtain unique BE sites

In a number of cases, different initial poses of the methanol molecule end up in the same final optimized structure. To avoid redundancies, which will affect the final BE distribution, we developed a pruning procedure. For a detailed discussion see Appendix A. Redundant sites are identified in the following way:

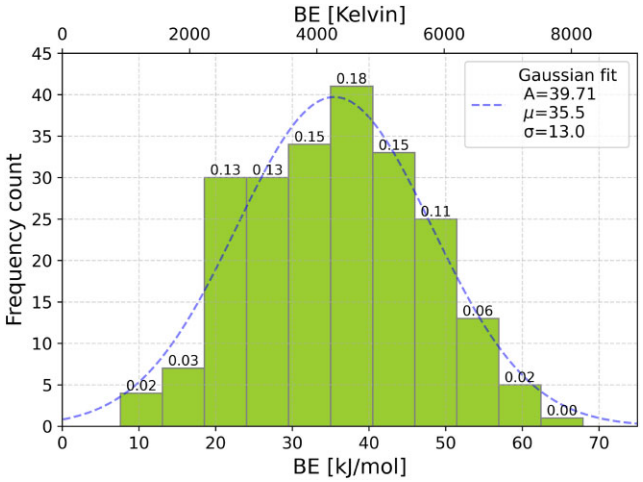

Figure 1. BSSE corrected BE distribution at DLPNO-CCSD(T) level. Structures and ZPEs are calculated at ONIOM(B97-3c:GFN2) level. The dashed curve is the $f_{\text{Gauss}}(\texttt{hist(BE)}, \sigma, \mu)$ not normalized Gaussian best-fitting function for the histogram.

(*i*) We select all the cases between BEs Model zone structures that have the same number of atoms,

(*ii*) For each case, we align the two structures and compute the absolute value of the energy difference $|\Delta E_{Cij}| = |E_{Ci} - E_{Cj}|$ between the *i* and *j*-esimal complex structure,

(*iii*) If the two structures have a root mean square deviation (RMSD) below 0.5 Å and $|\Delta E_{Cij}| < 1.0\,\text{kJ mol}^{-1}$ they are considered identical.

The selection of the pruning criteria (0.5 Å and $1.0\,\text{kJ mol}^{-1}$) is discussed in detail in Appendix A.

2.4 The desorption rate prefactor

As pointed out by previous articles (Ferrero et al. 2022; Minissale et al. 2022; Ceccarelli et al. 2023; Ligterink & Minissale 2023; Tinacci et al. 2023), attention should be given to the way in which the prefactor is computed in the desorption rate [$k_{\text{des}}^{\text{thermal}}$ in equation (7)]. As in the aforementioned articles, we here adopted the Tait et al. (2005) formula:

$$\nu(T) = \frac{k_{\text{B}}T}{h}\left(\frac{2\pi\, m\, k_{\text{B}}\text{T}}{h}\right) A\frac{\sqrt{\pi}}{\sigma h^3}\left(8\pi^2 k_{\text{B}}T\right)^{\frac{3}{2}}\sqrt{I_x\, I_y\, I_z}\,, \tag{5}$$

where k_{B} is the Boltzmann constant, T is the temperature, m the mass of the molecule, h the Planck constant, A is the surface area per adsorbed molecules (usually assumed to be 10^{-19} m^2), I_i is the adsorbate principal moment of inertia in the *i-esimal* direction, and σ is the symmetry adsorbate rotation factor. For CH_3OH, the principal moments of inertia are 3.92, 20.40, 21.10 a.m.u.Å^2, σ is 1 and m is 32.0419 a.m.u..

3 RESULTS

3.1 Binding energy distribution

After the pruning procedure, 263 redundant sites are identified and discarded from the distribution, resulting in 223 unique sites. All the obtained structures are PES minima, i.e. imaginary frequency are not present. The final distribution is reported in Fig. 1. The number of bins and their width are obtained following the Freedman Diaconis estimator (Freedman & Diaconis 1981). As shown in Fig. 1, the histograms fits well a Gaussian distribution:

$$G(\text{BE}) = A\exp\left(-\frac{(\text{BE}-\mu)^2}{2\sigma^2}\right), \tag{6}$$

where A is equal to 39.7, which represents the maximum height of the fitted Gaussian curve, the mean value of the BE μ is 35.5 kJ mol^{-1} (4255 K) and the standard deviation is 13.0 kJ mol^{-1} (1558 K). The maximum value found is 67.9 kJ mol^{-1}, while the lower is 7.6 kJ mol^{-1}. In Table 1, the relative population of each bin and the corresponding mean value are reported. The prefactor was computed at the desorption peak (T_{peak}) for the corresponding BE, solving numerically the Polany–Wigner equation (Polanyi & Wigner 1925), as done in a previous work by our group (Bariosco et al. 2024). T_{peak} is defined as the temperature at which the simulated TPD spectra exhibit the maximum desorption rate ($\frac{\text{dN}}{\text{dT}}$).

Table 1. Mean BE value, prefactor evaluated at the T_{peak} [$\nu(T_{\text{peak}})$], associated T_{peak} and relative population for each bin of the histogram (Fig. 1). Energy values reported in parenthesis are in Kelvin (K), while the others in kJ mol^{-1}. The prefactor is in s^{-1}. The bin width is 5.48 kJ mol^{-1} (659 K).

Mean BE value	$\nu(T_{\text{peak}})$	T_{peak}	Fraction of the ice
10.3 (1239)	2.62×10^{15}	33	0.02
15.8 (1898)	1.03×10^{16}	48	0.03
21.3 (2556)	2.58×10^{16}	63	0.13
26.8 (3214)	5.36×10^{16}	77	0.13
32.3 (3872)	9.81×10^{16}	92	0.15
37.8 (4530)	1.61×10^{17}	106	0.18
43.2 (5188)	2.46×10^{17}	119	0.15
48.7 (5846)	3.59×10^{17}	133	0.11
54.2 (6505)	5.03×10^{17}	146	0.06
59.7 (7163)	6.86×10^{17}	160	0.02
65.2 (7820)	9.12×10^{17}	173	0.004

3.2 BE decomposition and geometrical insights

As outlined in Section 2, BE represents a multicomponent term that may be dissected to enhance comprehension of the distribution's structure. In Fig. 2, the correlation plot between BE and several components such as BE$_e$(BSSE) (electronic BE without BSSE correction), δE_{def}, BSSE, and ΔZPE is illustrated. Along with, each point is associated with the number of water molecules in the QM zone and sketched in the coloured bar. The main outcomes can be summarized as follows:

(i) BE$_e$(BSSE) shows a strong correlation with the BE, and all the BE$_e$(BSSE) values, as expected, are higher than the respective BE ones. On the contrary, the number of water molecules in the QM zone do not correlate with the BE$_e$(BSSE);

(ii) The δE_{def} contribution is rather sparse, the majority being at low BE values (<20 kJ mol^{-1}), even if it slightly increases with the BE. A second mild direct correlation is the δE_{def} with the number of water molecules;

(iii) BSSE shows a clear increasing trend (with the majority of cases below 10 kJ mol^{-1}) with respect to the BE and, as expected, with the number of H_2O molecules in the Model Zone;

(iv) ΔZPE correction directly but sparsely correlates with BE. Although no clear correlation is observed between ΔZPE and the number of water molecules, ΔZPE generally increases as the size of the QM zone decreases.

Due to the crucial importance of low energy binding sites in this work, along with the energetics, we reported a deeper geometrical

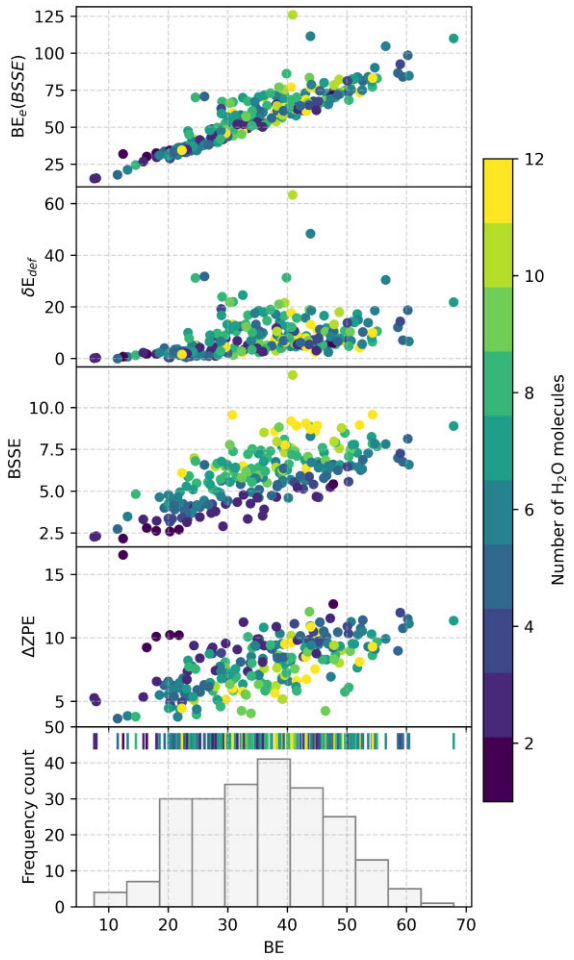

Figure 2. Correlation plot between BE and several contributions: electronic BE not corrected for BSSE (BE$_e$(BSSE)), deformation energy (δE_{def}), BSSE correction and ΔZPE. As in equation (2), BE = BE$_e$(BSSE) − δE_{def} − BSSE − ΔZPE. All energy values are in kJ mol^{-1} at DLPNO-CCSD(T)/aug-cc-pVTZ // B97-3c level. The colour map shows the number of H_2O molecules included in the Model region.

analysis on the methanol–water interaction. The H-bond cut-off criteria that we used, selected after an extensive visual check on the structures, are the following: ranges of 1.7–2.8 Å for the H-bond length, and 140–180° for the H-bond angle. In Fig. 3, the total distribution is divided into three distinct subgroups based on the number of H-bonds formed by CH_3OH: specifically, three H-bonds, two H-bonds, and one H-bond.

We remark that in each class, for instance that exhibiting three H-bonds, each case (O-acceptor, H-donor, C-donor) can contribute separately. Furthermore, the C-donor case is, to simplify notation, here improperly refereed to as H-bond when it should be more correctly described as a weak C-H donor bond. This interaction is also dominated by dispersion interactions. The reader can refer to the data base of all considered structures available in Section 5.1.

For each distribution, we linked the correlation plot between distance and angle for all H-bonds within the particular subclass. As reported in the first panel of Fig. 3, only 19 cases form three H-bonds, showing a BE average value of 45 kJ mol^{-1} and ranging from 31.4 to 67.9 kJ mol^{-1}. The two H-bonds class (second panel in Fig. 3) is the most populated one, spanning from 14.5 to 60.4 kJ mol^{-1} and with a BE mean value of 39.3 kJ mol^{-1}. Finally, with the 30 per cent of the total population, the one H-bond subclass (third panel of Fig. 3) varies from 7.9 to 46.4 kJ mol^{-1}, with an average BE value of 27.2 kJ mol^{-1}. In agreement with the expectations and previous simulations by our group (Tinacci et al. 2023; Bariosco et al. 2024), the higher the number of H-bonds the stronger the resulting BE.

In the right panels of Fig. 3, the associated features of the H-bonds established in the particular subclass are illustrated. As a common trend, irrespective of the considered subclass, the -CH_3 group act as weak H-bond donor (triangle marker), the majority of the cases being localized in the 2.5–2.8 Å range, while the -OH group as a medium-strength H-bond donor (circle marker) or acceptor (star marker), with a typical distance of 1.8–2.1 Å. On the contrary, when the -OH group act as an acceptor (circle marker in the right panels of Fig. 3), the structures are mainly confined between 1.8 to 2.1 Å (the typical distance of medium-strength H-bonds). A similar pattern is observed for the -OH group acting as a donor (star marker in the right panels of Fig. 3). Furthermore, as the number of H-bonds formed by CH_3OH increases, their geometric parameters become more dispersed. This dispersion may account for the moderate binding energies in the three H-bond subclass and the lower values in the two H-bond subclass.

4 DISCUSSION

4.1 Comparison with previous experimental results

From an experimental standpoint, the BE is computed indirectly through TPD measurements. With this technique the studied molecules are condensed on an inert cold finger and then the rate of desorption upon heating the sample is measured via quadrupole mass spectrometry. The thermal desorption of a species bound to a substrate can be approximately described by the Polanyi–Wigner equation (Polanyi & Wigner 1925), where the rate of desorption $k(T)$ is given by:

$$k(T) = -\frac{dN}{dT} = \frac{N^n}{\beta} \underbrace{\nu(T) \exp\left(-\frac{E_{des}}{RT}\right)}_{k_{des}^{thermal}}, \quad (7)$$

where N is the number (density) of molecules adsorbed on the surface, n is the order of the desorption, $k_{des}^{thermal}$ is the thermal desorption rate constant, ν is the pre-exponential factor (also called prefactor), T is the temperature of the surface, β is the surface heating rate ($\beta = \frac{dT}{dt}$), and E_{des} is the desorption energy, which coincide with the BE for non-activated desorption processes.

Many variables contribute to modify the desorption temperature of the species: the substrate (the cold finger), the coverage of the surface (sub, mono, or multilayer), the temperature ramp β and the prefactor adopted.

Table 2 shows the BE values of methanol extracted from TPD experiments, which range from 30.8 to 48 kJ mol^{-1} (3730–5770 K). As shown in Table 2, methanol adsorption experiments have been carried out on various substrates, of which only two using water-ice surfaces. Furthermore, the vast majority of these experiments occur in the multilayer regimes, where adsorbate–adsorbate interactions dominate over adsorbate–substrate interactions, causing the final BE to be biased by lateral interactions (Perrero et al. 2024). This may occur even at sub-monolayer regimes, when methanol molecules are not evenly spread over the substrate but coagulate and form multilayered clusters as reported for other adsorbates (Collings et al. 2015). Moreover, when the temperature ramp increases, E_{des} can also be biased by possible adsorbate re-organizations due to the proximity of the desorption temperature of the samples to their amorphous-to-

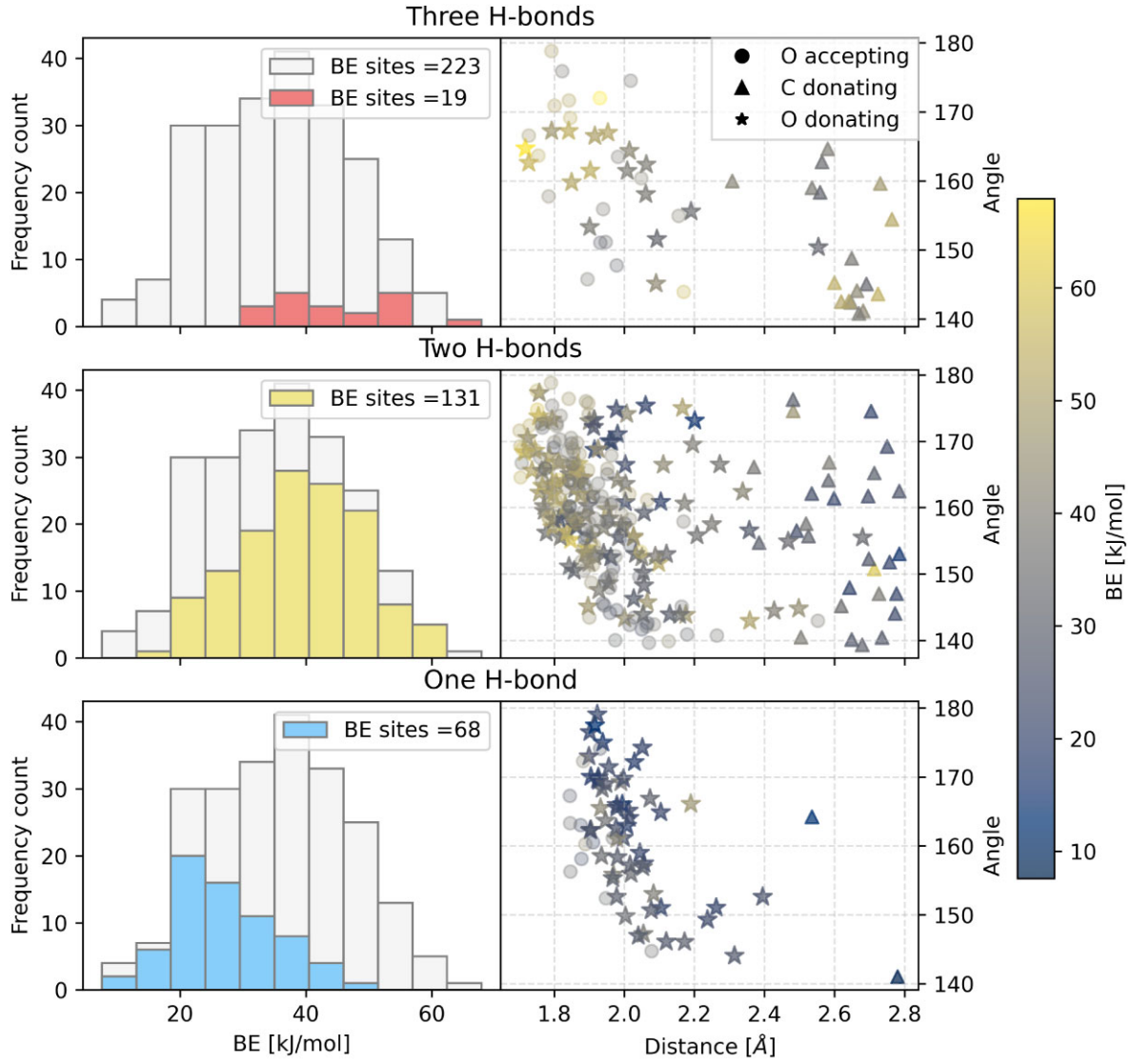

Figure 3. Correlation plot among various distributions characterized by the number of H-bonds formed by CH_3OH and the unique interaction features of each BE site. The left panel column displays the breakdown of the total distribution into three distinct classes based on the number of H-bonds established by CH_3OH: three, two, and one H-bond, arranged from top to bottom. The right-hand column illustrates the correlation plot between the H-bond distance and angle. Different markers represent CH_3OH acting as H-bond donor through the C atom (triangle), H-bond donor through the O atom (star), and H-bond acceptor through the O atom (circle). The colour mapping indicates the BE energy measured in kJ mol^{-1}.

crystalline phase transition (115–120 K for methanol) (Souda 2004; Burke & Brown 2015). For these reasons, a one-to-one comparison between computational and experimental BE should be treated with extreme care. To minimize the above problems, we have chosen the only two studies in the literature that use a water substrate to compare with our results.

The study by Bahr et al. (2008), conducted in the sub-monolayer regime, is the closest to our computational approach. Fig. 4 presents the simulated TPD spectra using the same prefactor as Bahr et al. (2008) (blue curve), along with the corresponding T_{peak} at 165 K (red line). As shown in Fig. 4, the computed T_{peak} occurs at 130 K, underestimating the value reported by Bahr et al. (2008). This discrepancy can be partially attributed to the co-desorption of water and methanol observed in the experimental procedure, a phenomenon that is not accounted for in our simulations (Bahr et al. 2008).

Another study on methanol adsorption on water surfaces is by Collings et al. (2004). The key difference between this work and Bahr et al. (2008) lies in the coverage regime: instead of the sub-monolayer regime as reported by Bahr et al. (2008) and Collings et al. (2004) examined methanol desorption in the multilayer regime, reporting a T_{peak} of 126 K. Surprisingly, the simulated TPD using the Tait et al. (2005) prefactor (green curve in Fig. 4) slightly underestimates the results of Collings et al. (2004) (orange line). This agreement looks somehow fortuitous given the different regime of the experiment (high coverage) compared to our simulations (zero coverage). While our model examines the interaction of a methanol molecule with an amorphous water ice surface, the experimental setup described by Collings et al. (2004) involves desorption of methanol from a methanol surface.

Nevertheless, the point here is to establish which adsorption regime is more representative of the ISM conditions. Given the ultra-low coverage assumed in our simulations and the low abundance of methanol with respect to water in the chemical composition of interstellar ices (Boogert et al. 2015), we propose that theoretical

Table 2. Values of the methanol BE in kJ mol^{-1} and K (in parenthesis) and prefactors as measured in literature experiments using different substrates, ice samples and methods.

METHANOL TPD EXPERIMENTS					
BE	T_{peak}	Prefactor	Substrate	Adsorbate ice sample	Ref.
46.4 ± 2.1 (5585 ± 252)	150	3.1×10^{24} [b]	Al_2O_3(0001)	Unspecified multilayer	1
33.0 − 48.0 (3970 − 5770)	144	Not indicated	HOPG	Monolayer	2
31.0 − 40.0 (3730 − 4810)	139	Not indicated	HOPG	Mixed multilayer	2
48.0 ± 3.0 (5770 ± 360)	147	$3 \times 10^{16\pm2}$ [b]	HOPG	Monolayer	3
46.0 ± 3.0 (5530 ± 360)	141	$3 \times 10^{16\pm2}$ [b]	HOPG	Unspecified multilayer	3
48.0 ± 0.8 (5773 ± 95)	Not reported	$9 \times 10^{9\pm3}$ [b]	HOPG	Monolayer	4
41.0 ± 0.8 (4931 ± 98)	Not reported	$6 \times 10^{25\pm3}$ [a]	HOPG	Unspecified multilayer	4
45.0 (5410)	165	1×10^{13} [b]	Amorphous D_2O	Sub-monolayer	5
43.2 ± 1.0 (5200 ± 120)	152	$3 \times 10^{30\pm1}$ [a]	Gold	Amorphous multilayer	6
44.1 ± 1.0 (5300 ± 120)	159	$3 \times 10^{30\pm1}$ [a]	Amorphous silicate	Amorphous multilayer	6
$36.2^{+1.7}_{-0.8}$ (4355^{+200}_{-100})	145	$5.3^{+16.0}_{-2.7} \times 10^{27}$ [a]	KBr	Unspecified multilayer	7
34.5 (4140)[c]	138	Not indicated	Oxidized graphite	Unspecified multilayer	8
31.8 ± 1.1 (3820 ± 135)[c]	128	Not indicated	Amorphous water	Unspecified multilayer	9–10

[a]zero order desorption (mol/cm^2 s^{-1}).
[b]first order desorption (s^{-1}).
[c]derived with empirical relation from Penteado, Walsh & Cuppen (2017).
References: [1] Nishimura, Gibbons & Tro (1998), [2] Bolina, Wolff & Brown (2005), [3] Ulbricht et al. (2006), [4] Brown & Bolina (2007), [5] Bahr, Toubin & Kempter (2008), [6] Green et al. (2009), [7] Martín-Doménech et al. (2014), [8] Minissale et al. (2016), [9] Penteado et al. (2017), [10] Collings et al. (2004).

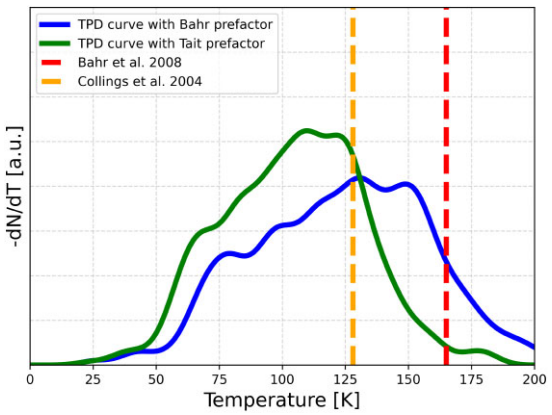

Figure 4. Comparison between simulated and experimental TPD spectra. The dashed lines represent the experimental T_{peak} reported by Collings et al. (2004) and Bahr et al. (2008), respectively. The continuous lines represent the summed TPD spectra for each value of BE computed in this work, fitted with a Gaussian function. The curve on the left is the simulated TPD using the Tait et al. (2005) prefactor, while the one on the right is the simulated TPD using the same prefactor adopted by Bahr et al. (2008), see Table 2. The heating rate (β) was fixed at 4 K min^{-1}, consistent with the experimental conditions of Collings et al. (2004).

BE computations may provide a more representative framework for modeling interstellar ices. Consequently, careful consideration is warranted when selecting specific BE values in numerical astrochemical models, as many experimental determinations predominantly reflect high-coverage conditions, which may not accurately capture the astrophysical context of molecular clouds.

4.2 Comparison with previous computational results

In this section, we juxtapose our findings with those existing in the literature, emphasizing the disparities and advancements relative to prior simulations. As a broad overview, the computed BEs for CH_3OH reported in Table 3 range from 26 to 71 kJ mol^{-1}, while our distribution goes from 7.9 to 67.9 kJ mol^{-1}. As in previous works where the ACO-FROST code was used, the main difference with respect to the literature is that our BE distributions are populated also at very low energy values. Three parameters influence the BE of a given species: (i) the selection of the surface model, (ii) the sampling methodology employed, and (iii) the specific computational method utilized.

Previous computed BE values can be classified into two main groups: cluster calculation, where the ice is approximated with a limited number of molecules, and periodic calculation, where the ice is treated as an infinite periodic amorphous or crystalline structure. In the former class, the number of considered water molecules is usually low (<22) with respect to our model in which 200 water molecules are included. Wakelam et al. (2017) issued two different values for methanol acting as H-bond donor (37.4 kJ mol^{-1}, 4500 K) or H-bond acceptor (42.4 kJ mol^{-1}, 5100 K). Although a good match can be found with our values, the single water molecule used by Wakelam et al. (2017) is too simple to represent the amorphousness of an icy grain. A similar work devoted to understand the effect of the number of molecules included in the surface was done by Das et al. (2018). The cluster surface was extended from one to six water molecules and the BEs computed accordingly. The BE correlates with the size of the surface going from 26 (3124 K) to 37.5 kJ mol^{-1} (4511 K), showing that previously published BEs are not converged, and more molecules are needed for the correct description of the water surface. A good improvement towards a statistically meaningful distribution is represented by the recent work from Bovolenta et al. (2022) that considered 20 water clusters, each consisting of 22 molecules, also including ZPE and BSSE corrections. They reported two main binding modes, methanol acting as H-bond acceptor with a mean value of 19.5 kJ mol^{-1} (2344 K) and as H-bond donor with a mean value of 26.9 kJ mol^{-1} (3235 K), while the maximum value of the distribution falls at around 44 kJ mol^{-1} (5300 K). As regards the simulation of extended surfaces, three different works have been devoted to the interaction of methanol

Table 3. Values of the methanol BE as computed in different theoretical studies using various methods and ice grain models. Units are in kJ mol^{-1} and K, for the values in parenthesis. Max and Min are maximum and minimum values, μ is the distribution's mean, and σ the standard deviation.

	METHANOL SIMULATIONS		
BE	Ice model	Method	Ref.
One H-bond: 31.0 (3730) **Two H-bond:** 54.0 (6490) μ: 47.25 (5683)	Submonolayer on crystalline periodic	TIP5P	1
39.94 (4804)	Monolayer on crystalline periodic	TIP5P	1
60.0 (7220)	Crystalline periodic	TIP4P	2
H-bond donor: 37.4 (4500)	Water monomer	M06-2X/aug-cc-pvtz[c]	3
H-bond receiver: 42.4 (5100)			
26.0 (3124)	Water monomer	MP2/aug-cc-pvdz[b]	4
32.6 (3924)	Water trimer	MP2/aug-cc-pvdz[b]	4
36.3 (4368)	Water tetramer	MP2/aug-cc-pvdz[b]	4
38.3 (4607)	Water pentamer	MP2/aug-cc-pvdz[b]	4
37.5 (4511)	Water hexamer	MP2/aug-cc-pvdz[b]	4
Max: 44.3 (5331) **μ H-bond donor:** 26.9 (3235) **μ H-bond acceptor:** 19.5 (2344)	Amorphous cluster (22 H_2O)	ω-PBE/def2-TZVP // HF-3c	5
61.4 (7385)	Crystalline periodic	B3LYP-D3/A-VTZ[a]	6
Min: 31.3 (3770) Max: 71.7 (8618) μ: 53.3 (6412)	Amorphous periodic (60 H_2O)	B3LYP-D3/A-VTZ // HF-3c[a]	6
Min: 7.6 (914) Max: 67.9 (8167) μ: 35.5 (4270)	Iced grain (200 H_2O)	ON(DLPNO-CCSD(T)/aug-cc-pvtz:GFN2) // ON(B97-3C:GFN2)	This work

[a]A-VTZ refers to Ahlrichs triple zeta basis set augmented with two polarization functions.
[b]BSSE and ZPE corrections not applied.
References: [1] Jedlovszky et al. (2006), [2] Bahr et al. (2008), [3] Wakelam et al. (2017), [4] Das et al. (2018), [5] Bovolenta et al. (2022), [6] Ferrero et al. (2020).

onto periodic water surfaces (Jedlovszky et al. 2006; Bahr et al. 2008; Ferrero et al. 2020). Jedlovszky et al. (2006) studied the adsorption isotherm of methanol on crystalline ice considering both the sub- and monolayer regimes. In the former case, which is the one that bears more resemblance to our work, the authors reported two different BE values: 31.0 kJ mol^{-1} (3730 K) and 54.0 kJ mol^{-1} (6490 K) when one or two H-bonds are established by methanol with the surface, which are overestimated with respect to our data: 27.2 and 39.3 kJ/mol kJ mol^{-1}, respectively. Bahr et al. (2008) published a similar work but considering a crystalline surface with a BE value of 60 kJ mol^{-1}. In our work, only 2 per cent of the BE sites populates such high values in the distribution (see Fig. 1 bottom panel); this is consistent with the fact that the H-bond cooperativity is maximized in a crystalline structure (Schaff & Roberts 1996), as also reported by Ferrero et al. (2020) (61.4 kJ mol^{-1}). Differently, the BE range obtained on the amorphous surface goes from 31.3 (3770 K) to 71.7 (8618 K) kJ mol^{-1} with a mean value of 53.3 kJ mol^{-1} (6412 K). The mean value of Ferrero et al. (2020) is almost 20 kJ mol^{-1} higher with respect to the one illustrated in this work. The discrepancies with the present results can be attributed to several factors: (i) the use of a different icy surface model (the grain was constructed by merging three smaller clusters), (ii) the use of a low-accuracy HF-3c level for geometry optimizations, (iii) the approximations applied to ZPE and CCSD(T) [see Bariosco et al. (2024) for more details], and (iv) the limited number of BE sites selected manually, which were biased by the chemical intuition.

In conclusion, our computed BE distribution shows good agreement with studies that incorporate statistically robust methods, such as Bovolenta et al. (2022), which reported BE modes consistent with the low-energy tail of our distribution. However, discrepancies exist with works like Jedlovszky et al. (2006), where their crystalline surface overestimated BEs compared to our values. Similarly, the higher mean BE values reported by Ferrero et al. (2020) can be attributed to differences in surface models, low-accuracy geometry optimizations, and limited sampling of BE sites. Our results provide an improved representation by including low-energy contributions often overlooked in earlier studies, as discussed in the following Sections, while highlighting methodological limitations in other works.

4.3 Astrochemical implication of methanol BE distribution

4.3.1 Thermal desorption

Since the first detection of gaseous methanol in cold molecular clouds, its origin has puzzled astrochemists (Friberg et al. 1988). As discussed in the Introduction, a pure gas-phase route of methanol formation fails to reproduce the observed abundances, of a few 10^{-9} with respect to H_2, (e.g. Rodgers & Charnley 2001; Garrod et al. 2006; Geppert et al. 2006). Nowadays, it is assumed that methanol is actually formed on the dust grain surfaces by the successive addition of H atoms to frozen CO (e.g. Watanabe & Kouchi 2002; Rimola et al. 2014), in agreement with the observations of frozen methanol in cold environments where also CO is largely frozen (e.g. Boogert et al. 2015; McClure et al. 2023).

While the formation of methanol on grain surfaces solves the problem in warm objects, it does not in cold environments where the dust is not warm enough for methanol to be thermally desorbed.

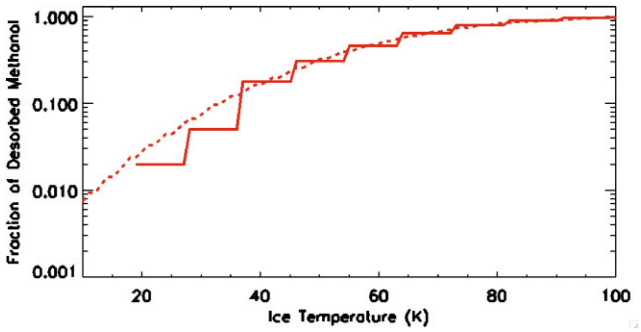

Figure 5. Fraction of the desorbed methanol frozen on a water ice surface as a function of the ice temperature. The solid line is computed using the Table 1 data while the dashed line uses the Gaussian fit of equation (6).

Usually, it is assumed that non-thermal desorption injects a fraction of frozen methanol into the gas-phase, where it is observed via rotational lines. As discussed in the Introduction, the generally assumed mechanism is that of CD, whose efficiency for methanol is not well constrained (Minissale et al. 2016; Ligterink et al. 2018; Pantaleone et al. 2020).

Our calculations of the methanol BE distribution shed new light on the possible mechanism responsible for the injection of frozen methanol into the gas-phase. Fig. 1 and Table 1 show that about 2 per cent of frozen methanol is in sites with BE around 1200 K, opening the possibility that a similar fraction of methanol ice is injected into the gas-phase at temperatures relatively low.

To have an approximate value of the ice temperature (which is, obviously, equal to the dust temperature) at which a frozen species desorbs, $T_{\rm des}$, one can consider the half lifetime $\tau_{1/2}$ of the species on an ice at $T_{\rm des}$, which is given by:

$$\tau_{1/2} = \frac{\ln(2)}{k_{\rm des}^{\rm thermal}}, \tag{8}$$

where the desorption rate $k_{\rm des}^{\rm thermal}$ is given by equation (7) with $n = 1$:

$$k_{\rm des}^{\rm thermal} = \upsilon_{\rm des}(T_{\rm peak}) \exp\left(-\frac{\rm BE}{T_{\rm des}}\right) \tag{9}$$

with BE in Kelvin and $\upsilon_{\rm des}$ in $\rm s^{-1}$. Where $T_{\rm peak}$ is the simulated desorption temperature obtained by numerically solving the Polany–Wigner equation (Polanyi & Wigner 1925). Inverting equation (8) provides the desorption temperature $T_{\rm des}$ as a function of BE for a given ice age $t_{\rm ice}$ (which is equal to $\tau_{1/2}$) and temperature $T_{\rm des}$:

$$T_{\rm des} = {\rm BE}\left[ln\left(\frac{\upsilon_{\rm des}(T_{\rm peak})}{ln2}\, t_{\rm ice}\right)\right]^{-1}. \tag{10}$$

Fig. 5 shows the fraction of desorbed ice as a function of the ice temperature $T_{\rm ice}$, assuming an ice age of 1 Myr and using the values of BE and $\upsilon_{\rm des}$ from Table 1 and the Gaussian function of equation (6) (and with $\upsilon_{\rm des}$ extrapolated from Table 1), respectively.

As anticipated, about 2 per cent of frozen methanol is thermally desorbed at dust temperatures as low as 18–25 K, using the lowest BE bin of Table 1. Fig. 5 also shows the extrapolation at lower temperatures using the Gaussian function that best fits the obtained BE distribution. Using this extrapolation, it is predicted that about 0.8 per cent of frozen methanol is desorbed at 10 K. Obviously, in order to have a more reliable number, simulations on a larger ice grain are mandatory to increase the statistics of the low BE sites. However, it seems more than reasonable to state that thermal desorption of methanol can occur also at low, previously unexpected temperatures and explain the measurement of the gaseous methanol abundance in cold environments. For example, assuming a frozen methanol abundance of 10^{-6}–10^{-5}, as measured in the interstellar ices (e.g. Boogert et al. 2015; McClure et al. 2023), it would be enough that about 0.01–0.1 per cent of ice is desorbed into the gas-phase to explain its observed abundance, $\sim 10^{-12}$–10^{-9} (see below), in cold environments. The upper end (0.1 per cent) is about what is predicted by using the Gaussian that fits the methanol BE distribution, which suggests that thermal desorption from the low-end BE sites could explain the observed abundances. This is by considering conditions represented by our atomistic modelling approach, namely, that methanol is formed (and subsequently thermally desorbed) on predominantly water-rich icy grains. If the ices contain frozen CO, for example, the BE may even be lower (e.g. Molpeceres et al. 2021; Ferrari et al. 2023). Whether the low-end BE sites can indeed solve the conundrum of gaseous methanol in cold environments depends on how exactly the desorption process takes place. Specifically, the higher BE sites could be more populated than the lower ones with respect to the statistical distribution here computed. Computing the actual population of the sites requires an ad hoc ab initio modelling beyond the scope of this work.

These considerations/explanations apply to a variety of objects where the dust temperature is relatively low and previously not considered enough for thermal desorption to occur. Two classes of objects are particularly relevant: prestellar cores and protoplanetary discs. The study by Punanova et al. (2022), for example, reports the maps of gaseous methanol towards seven prestellar cores of the L1495 filamentary structure in the Taurus molecular complex. As in other studies (e.g. Bizzocchi et al. 2014; Vastel et al. 2014; Spezzano et al. 2020), methanol is distributed in shells surrounding the core centres, where the CO depletion is present but not extreme, at a visual extinction $A_{\rm v} = 5$–10 mag, where the dust temperature is around 11–13 K (Punanova et al. 2022). The derived methanol abundances ranges between 0.5 and 8.5 $\times 10^{-9}$. Punanova et al. (2022) modelled their observations with the laudable aim of constraining the parameters of the CD, assumed to be responsible for the gaseous methanol. These authors did not have the information of a methanol BE distribution, so their assumption was the most reasonable at the time. However, our new calculations of the BE distribution point out that thermal desorption of frozen methanol could be the mechanism at work.

Another class of cold objects where methanol has been observed in the gas-phase are the protoplanetary discs (Walsh et al. 2016; Lee et al. 2022; Öberg, Facchini & Anderson 2023; Yamato et al. 2024). Also in these cases, and specifically in the 'classical' cold protoplanetary disc TW Hya (Walsh et al. 2016), the dust temperature, where gaseous methanol is observed, is relatively low ($\leq$15 K) as it is the methanol abundance, $\sim 10^{-12}$–10^{-11}. As for the prestellar cores, the low-end of the methanol BE distribution is more than enough to explain the presence of gaseous methanol also in TW Hya and, more generally, in protoplanetary discs.

To summarize, our new calculations may solve a decades-long puzzle as to why gaseous methanol exists in cold environments where thermal desorption was thought to be completely inefficient.

4.3.2 *Chemical desorption*

The BE distribution also affects the CD efficiency. Indeed, if an exothermic reaction occurs at low-energy binding sites, the released kinetic energy absorbed by the newly formed molecule can be large enough for the latter to be liberated in the gas-phase. This is the case, for example, of hydrogen sulphide (H_2S) (Oba et al. 2018), where

Table 4. Absolute enthalpies at 0 K are reported for the species involved in the reaction CH3O$^{\cdot}$ + H$^{\cdot}$ → CH_3OH. All the absolute values are in Hartree (1 Hartree = 2625.5 kJ mol^{-1}), while the energy difference is reported in kJ mol^{-1}. In the last line, the reaction enthalpy computed as $\sum H_{prod}(0\ K) - \sum H_{react}(0\ K)$ is shown. Geometries and frequencies are calculated at B97-3c level. DLPNO-CCSD(T) method is coupled with the aug-cc-pVTZ basis set. The superscript '·' identifies the open-shell species.

Species	DLPNO-CCSD(T)//B97-3C
H$^{\cdot}$ (doublet)	0.4998
CH3O$^{\cdot}$ (doublet)	114.8488
CH_3OH	115.5113
$\Delta_r H^{\circ}$ (CH_3OH)	427.1

the BEs are low with respect to the energy left to the H_2S formed by the H addition to HS on the grain surfaces (Bariosco et al. 2024).

To estimate what happens to a CH_3OH molecule formed on the grain surfaces by the H addition to CH_3O, one can consider the enthalpy of the reaction. Based on our previous studies that used AIMD simulations (Pantaleone et al. 2020, 2021; Ferrero et al. 2023), we can assume that about 10–50 per cent of the reaction energy remains to the newly formed molecule (see also the discussion in Bariosco et al. 2024). Our *ad hoc* calculations, reported in Table 4, indicate that the CH_3O + H reaction enthalpy is equal to 427 kJ mol^{-1}. Therefore, a newly formed CH_3OH would have about 40–200 kJ mol^{-1}, to compare with the BE distribution of Fig. 1, whose mean is 35.5 kJ mol^{-1}. The energy retained by the newly formed CH_3OH molecule may be enough, in the sites with BE much lower than 40–200 kJ mol^{-1}, to liberate it into the gas-phase, but the efficiency of the process is not as large as H_2S, for which the BE mean is 7.5 kJ mol^{-1}, in agreement with the earlier conclusions by Pantaleone et al. (2020). Dedicated AIMD simulations are necessary to better estimate the entity of the CD for the methanol case.

5 CONCLUSION

We reported new QM calculations of the BE distribution of methanol on a ice surface, leveraging on previous works by our group (Germain et al. 2022; Tinacci et al. 2022, 2023; Bariosco et al. 2024). The main results of the present work are:

(i) The adopted amorphous ice surface is made of 200 water molecules, on which we obtained 223 unique binding sites. The obtained BE distribution is well described by a Gaussian function with a mean of 35.5 kJ mol^{-1} (4255 K) and a standard deviation of 13.0 kJ mol^{-1} (1558 K).

(ii) The calculated range of methanol BEs (7.9–67.9 kJ mol^{-1}) is in agreement with previous laboratory experiments and theoretical calculations estimates of BE (single values).

(iii) The low-energy end of the methanol BE distribution may explain the presence of gaseous methanol also in cold environments, such as prestellar cores and protoplanetary discs. Specifically, 2 per cent of the BEs are equal to ∼10 kJ mol^{-1} (∼1240 K). Using a simple calculation of the lifetime of frozen methanol on an icy surface predicts that up to 0.8 per cent of frozen methanol is desorbed at ice temperatures of 10 K. Considering that the abundance of frozen methanol is measured to be $\sim 10^{-6}$–10^{-5}, thermal evaporation of even such a small fraction of low BEs can reproduce the gaseous methanol abundance of $\leq 10^{-8}$ measured in cold environments.

(iv) The low-energy end of the BE distribution also impacts the quantity of methanol liberated from the icy surfaces when it is formed by H addition of CH_3O, the so-called CD efficiency. However, in order to provide specific values, dedicated AIMDs simulations are necessary.

(v) Given the huge impact that the low-end BE distribution has on the gaseous methanol abundance in cold environments, it is of paramount importance to obtain BE calculations on grains with a larger number of water molecules than those in this study (200).

We conclude by emphasizing the importance of obtaining the most accurate possible description of the processes responsible of the observed chemical interstellar richness, which may solve decades-long puzzles, like the presence of gaseous methanol in cold environments, without the necessity of unconstrained processes.

ACKNOWLEDGEMENTS

This project has received funding within the European Union's Horizon 2020 research and innovation programme from the European Research Council (ERC) for the projects 'The Dawn of Organic Chemistry' (DOC), grant agreement no. 741002, 'Quantum Chemistry on Interstellar Grains' (QUANTUMGRAIN), grant agreement no. 865657, and from the Marie Skłodowska-Curie for the project'Astro-Chemical Origins' (ACO), grant agreement no. 811312. In the context of the ACO project, we thank Aurèle Germain for preliminary XTB-GFN2 calculations and for searching literature experimental and theoretical BE data for methanol. PU and SP acknowledge the Italian Space Agency for co-funding the Life in Space Project (ASI N. 2019-3-U.O), the Italian MUR (PRIN 2020, Astrochemistry Beyond the Second Period Elements, Prot. 2020AFB3FX), PU acknowledges also support from Project CH4.0 under the MUR programme 'Dipartimenti di Eccellenza 20232027' (CUP: D13C22003520001). We acknowledge the EuroHPC Joint Undertaking for awarding this project access to the EuroHPC supercomputer LUMI, hosted by CSC (Finland) and the LUMI consortium through the EuroHPC. AR acknowledges MICIN for the projects PID2021-126427NBI00 and CNS2023-144902. AR gratefully acknowledges support through 2023 ICREA Award. LT is grateful to Stefano Ferrero for insightful discussions. Finally, we wish to acknowledge the extremely useful discussions with Prof. Gretobape.

DATA AVAILABILITY

To easily handle the large data set of BE samples (atomic coordinates and BE values), we developed and made public available a web site based on the molecule hyperactive JSmol plugin (Jmol: an open-source Java viewer for chemical structures in 3D[1]).

The extended electronic version of the calculated results, including all the 223 sample optimized structures at ONIOM(B97-3c/aug-cc-pVTZ:xTB-GFN2) level, are available at https://tinaccil.github.io/Jmol_BE_CH3OH_visualization/. All the structures and binding energies data set are available in Zenodo.

REFERENCES

Aikawa Y., Furuya K., Yamamoto S., Sakai N., 2020, ApJ, 897, 110
Bachiller R., Liechti S., Walmsley C. M., Colomer F., 1995, A&A, 295, L51 https://ui.adsabs.harvard.edu/abs/1995A

[1]http://www.jmol.org/

Bahr S., Toubin C., Kempter V., 2008, J. Chem. Phys., 128, 134712
Ball J. A., Gottlieb C. A., Lilley A. E., Radford H. E., 1970, ApJ, 162, L203
Bannwarth C., Ehlert S., Grimme S., 2019, J. Chem. Theory Comput., 15, 1652
Bariosco V., Pantaleone S., Ceccarelli C., Rimola A., Balucani N., Corno M., Ugliengo P., 2024, MNRAS, 531, 1371
Bergner J. B., Öberg K. I., Rajappan M., 2017, ApJ, 845, 29
Bertin M. et al., 2016, ApJ, 817, L12
Bisschop S. E., Jørgensen J. K., van Dishoeck E. F., de Wachter E. B. M., 2007, A&A, 465, 913
Bizzocchi L., Caselli P., Spezzano S., Leonardo E., 2014, A&A, 569, A27
Blake G. A., Sutton E. C., Masson C. R., Phillips T. G., 1987, ApJ, 315, 621
Bockelee-Morvan D., Colom P., Crovisier J., Despois D., Paubert G., 1991, Nature, 350, 318
Bolina A. S., Wolff A. J., Brown W. A., 2005, J. Phys. Chem. B., 109, 16836
Boogert A. C. A., Gerakines P. A., Whittet D. C. B., 2015, ARA&A, 53, 541
Bottinelli S. et al., 2010, ApJ, 718, 1100
Bovolenta G. M., Vogt-Geisse S., Bovino S., Grassi T., 2022, ApJS, 262, 17
Boys S. F., Bernardi F., 1970, Mol. Phys., 19, 553
Brandenburg J. G., Bannwarth C., Hansen A., Grimme S., 2018, J. Chem. Phys., 148, 064104
Brown W. A., Bolina A. S., 2007, MNRAS, 374, 1006
Burke D. J., Brown W. A., 2015, MNRAS, 448, 1807
Caselli P., Hartquist T. W., Havnes O., 1997, A&A, 322, 296
Cazaux S., Tielens A. G. G. M., Ceccarelli C., Castets A., Wakelam V., Caux E., Parise B., Teyssier D., 2003, ApJ, 593, L51
Ceccarelli C. et al., 2017, ApJ, 850, 176
Ceccarelli C. et al., 2023, ASP Conf. Ser. Vol. 534, Protostars and Planets VII. Astron. Soc. Pac., San Francisco, p. 379
Chaabouni H., Diana S., Nguyen T., Dulieu F., 2018, A&A, 612, A47
Chahine L. et al., 2022a, A&A, 657, A78
Chahine L. et al., 2022b, A&A, 667, A6
Chahine L. et al., 2024, MNRAS, 531, 2653
Charnley S. B., Kress M. E., Tielens A. G. G. M., Millar T. J., 1995, ApJ, 448, 232
Chen Y. et al., 2023, A&A, 678, A137
Chen Y. et al., 2024, A&A, 690, A205
Chuang K. J., Fedoseev G., Qasim D., Ioppolo S., van Dishoeck E. F., Linnartz H., 2018, ApJ, 853, 102
Codella C. et al., 2020, A&A, 635, A17
Collings M. P., Anderson M. A., Chen R., Dever J. W., Viti S., Williams D. A., McCoustra M. R. S., 2004, MNRAS, 354, 1133
Collings M. P., Frankland V. L., Lasne J., Marchione D., Rosu-Finsen A., McCoustra M. R. S., 2015, MNRAS, 449, 1826
Cummins S. E., Linke R. A., Thaddeus P., 1986, ApJS, 60, 819
Dartois E., Chabot M., Bacmann A., Boduch P., Domaracka A., Rothard H., 2020, A&A, 634, A103
Das A., Sil M., Gorai P., Chakrabarti S. K., Loison J. C., 2018, ApJS, 237, 9
Duley W. W., Williams D. A., 1993, MNRAS, 260, 37
Faggi S., Lippi M., Mumma M. J., Villanueva G. L., 2023, Planet. Sci. J., 4, 8
Ferrari B. C., Molpeceres G., Kästner J., Aikawa Y., van Hemert M., Meyer J., Lamberts T., 2023, ACS Earth Space Chem., 7, 1423
Ferrero S., Zamirri L., Ceccarelli C., Witzel A., Rimola A., Ugliengo P., 2020, ApJ, 904, 11
Ferrero S. et al., 2022, MNRAS, 516, 2586
Ferrero S., Pantaleone S., Ceccarelli C., Ugliengo P., Sodupe M., Rimola A., 2023, ApJ, 944, 142
Freedman D., Diaconis P., 1981, Z. Wahrscheinlichkeit., 57, 453
Friberg P., Madden S. C., Hjalmarson A., Irvine W. M., 1988, A&A, 195, 281
Fuchs G. W., Cuppen H. M., Ioppolo S., Romanzin C., Bisschop S. E., Andersson S., van Dishoeck E. F., Linnartz H., 2009, A&A, 505, 629
Garrod R., Hee Park I., Caselli P., Herbst E., 2006, Faraday Discuss., 133, 51
Garrod R. T., Wakelam V., Herbst E., 2007, A&A, 467, 1103
Geppert W. D. et al., 2006, Faraday Discuss., 133, 177
Germain A., Tinacci L., Pantaleone S., Ceccarelli C., Ugliengo P., 2022, ACS Earth Space Chem., 6, 1286
Green S. D., Bolina A. S., Chen R., Collings M. P., Brown W. A., McCoustra M. R. S., 2009, MNRAS, 398, 357
Grim R. J. A., Baas F., Geballe T. R., Greenberg J. M., Schutte W. A., 1991, A&A, 243, 473
Grimme S., Bannwarth C., Shushkov P., 2017, J. Chem. Theory Comput., 13, 1989
Guo Y., Riplinger C., Becker U., Liakos D. G., Minenkov Y., Cavallo L., Neese F., 2018, J. Chem. Phys., 148, 011101
Gusdorf A., Pineau Des Forêts G., Cabrit S., Flower D. R., 2008, A&A, 490, 695
Harada N., Sakamoto K., Martín S., Watanabe Y., Aladro R., Riquelme D., Hirota A., 2019, ApJ, 884, 100
Herbst E., van Dishoeck E. F., 2009, ARA&A, 47, 427
Hidaka H., Watanabe N., Shiraki T., Nagaoka A., Kouchi A., 2004, ApJ, 614, 1124
Jedlovszky P., Pártay L., Hoang P. N. M., Picaud S., von Hessberg P., Crowley J. N., 2006, J. Am. Chem. Soc., 128, 15300
Kakkenpara Suresh S., Dulieu F., Vitorino J., Caselli P., 2024, A&A, 682, A163
Kalvāns J., 2021, ApJ, 910, 54
Kendall R. A., Dunning Jr T. H., Harrison R. J., 1992, J. Chem. Phys, 96, 6796
Lee C.-F., Codella C., Ceccarelli C., López-Sepulcre A., 2022, ApJ, 937, 10
Ligterink N. F. W., Minissale M., 2023, A&A, 676, A80
Ligterink N. F. W., Walsh C., Bhuin R. G., Vissapragada S., Terwisscha van Scheltinga J., Linnartz H., 2018, A&A, 612, A88
Lippi M., Podio L., Codella C., Faggi S., De Simone M., Villanueva G. L., Mumma M. J., Ceccarelli C., 2024, ApJ, 970, L5
Maret S., Ceccarelli C., Tielens A. G. G. M., Caux E., Lefloch B., Faure A., Castets A., Flower D. R., 2005, A&A, 442, 527
Martín-Doménech R., Muñoz Caro G. M., Bueno J., Goesmann F., 2014, A&A, 564, A8
Martín S., Martín-Pintado J., Mauersberger R., 2006, A&A, 450, L13
Martinez-Bachs B., Anguera-Gonzalez A., Pareras G., Rimola A., 2024a, ChemPhysChem, 25, e202400272
Martínez-Bachs B., Ferrero S., Ceccarelli C., Ugliengo P., Rimola A., 2024b, ApJ, 969, 63
May P. W., Pineau des Forêts G., Flower D. R., Field D., Allan N. L., Purton J. A., 2000, MNRAS, 318, 809
Mayhall N. J., Raghavachari K., Hratchian H. P., 2010, J. Chem. Phys., 132, 114107
McClure M. K. et al., 2023, Nat. Astron., 7, 431
Menten K. M., Walmsley C. M., Henkel C., Wilson T. L., 1988, A&A, 198, 253
Minissale M., Moudens A., Baouche S., Chaabouni H., Dulieu F., 2016, MNRAS, 458, 2953
Minissale M. et al., 2022, ACS Earth Space Chem., 6, 597
Molpeceres G., Zaverkin V., Watanabe N., Kästner J., 2021, A&A, 648, A84
Nakai Y., Sameera W. M. C., Furuya K., Hidaka H., Ishibashi A., Watanabe N., 2023, ApJ, 953, 162
Neese F., 2022, Wires Comput. Mol. Sci., 12, e1606
Nishimura S. Y., Gibbons R. F., Tro N. J., 1998, J. Phys. Chem. B, 102, 6831
Oba Y., Tomaru T., Lamberts T., Kouchi A., Watanabe N., 2018, Nat. Astron., 2, 228
Öberg K. I., Bottinelli S., Jørgensen J. K., van Dishoeck E. F., 2010, ApJ, 716, 825
Öberg K. I., Facchini S., Anderson D. E., 2023, ARA&A, 61, 287
Pantaleone S., Enrique-Romero J., Ceccarelli C., Ugliengo P., Balucani N., Rimola A., 2020, ApJ, 897, 56
Pantaleone S., Enrique-Romero J., Ceccarelli C., Ferrero S., Balucani N., Rimola A., Ugliengo P., 2021, ApJ, 917, 49
Pareras G., Cabedo V., McCoustra M., Rimola A., 2023, A&A, 680, A57
Penteado E. M., Walsh C., Cuppen H. M., 2017, ApJ, 844, 71

Perrero J., Enrique-Romero J., Ferrero S., Ceccarelli C., Podio L., Codella C., Rimola A., Ugliengo P., 2022, ApJ, 938, 158
Perrero J., Vitorino J., Congiu E., Ugliengo P., Rimola A., Dulieu F., 2024, Phys. Chem. Chem. Phys, 26, 18205
Pineau des Forets G., Roueff E., Schilke P., Flower D. R., 1993, MNRAS, 262, 915
Polanyi M., Wigner E., 1925, Z. Angew. Phys., 33, 429
Potapov A., Krasnokutski S. A., Jäger C., Henning T., 2021, ApJ, 920, 111
Punanova A., Vasyunin A., Caselli P., Howard A., Spezzano S., Shirley Y., Scibelli S., Harju J., 2022, ApJ, 927, 213
Qasim D., Chuang K. J., Fedoseev G., Ioppolo S., Boogert A. C. A., Linnartz H., 2018, A&A, 612, A83
Rimola A., Taquet V., Ugliengo P., Balucani N., Ceccarelli C., 2014, A&A, 572, A70
Rodgers S. D., Charnley S. B., 2001, ApJ, 546, 324
Santos J. C., Chuang K.-J., Lamberts T., Fedoseev G., Ioppolo S., Linnartz H., 2022, ApJ, 931, L33
Schaff J. E., Roberts J. T., 1996, J. Phys. Chem., 100, 14151
Schilke P., Walmsley C. M., Pineau des Forets G., Flower D. R., 1997, A&A, 321, 293
Scibelli S., Shirley Y., 2020, ApJ, 891, 73
Shingledecker C. N., Lamberts T., Laas J. C., Vasyunin A., Herbst E., Kästner J., Caselli P., 2020, ApJ, 888, 52
Smith I. W. M., Herbst E., Chang Q., 2004, MNRAS, 350, 323
Song L., Kästner J., 2017, ApJ, 850, 118
Souda R., 2004, Phys. Rev. Lett., 93, 235502
Spezzano S., Caselli P., Pineda J. E., Bizzocchi L., Prudenzano D., Nagy Z., 2020, A&A, 643, A60
Spezzano S. et al., 2022, A&A, 657, A10
Tait S. L., Dohnálek Z., Campbell C. T., Kay B. D., 2005, J. Chem. Phys., 122, 164708
Taquet V., Ceccarelli C., Kahane C., 2012, A&A, 538, A42
Taquet V., López-Sepulcre A., Ceccarelli C., Neri R., Kahane C., Charnley S. B., 2015, ApJ, 804, 81
Taquet V., Wirström E. S., Charnley S. B., 2016, ApJ, 821, 46
Tinacci L., Germain A., Pantaleone S., Ferrero S., Ceccarelli C., Ugliengo P., 2022, ACS Earth Space Chem., 6, 1514
Tinacci L., Germain A., Pantaleone S., Ceccarelli C., Balucani N., Ugliengo P., 2023, ApJ, 951, 32
Tsuge M., Watanabe N., 2023, Proc. Japan Acad. B, 99, 103
Ulbricht H., Zacharia R., Cindir N., Hertel T., 2006, Carbon, 44, 2931
Van der Tak F. F. S., van Dishoeck E. F., Caselli P., 2000, A&A, 361, 327
Vastel C., Ceccarelli C., Lefloch B., Bachiller R., 2014, ApJ, 795, L2
Vastel C. et al., 2022, A&A, 664, A171
Wakelam V., Loison J. C., Mereau R., Ruaud M., 2017, Mol. Astrophys., 6, 22
Wakelam V., Dartois E., Chabot M., Spezzano S., Navarro-Almaida D., Loison J. C., Fuente A., 2021, A&A, 652, A63
Walsh C. et al., 2016, ApJ, 823, L10
Watanabe N., Kouchi A., 2002, ApJ, 571, L173
Weigend F., Köhn A., Hättig C., 2002, J. Chem. Phys., 116, 3175
Willacy K., Rawlings J. M. C., Williams D. A., 1994, MNRAS, 269, 921
Woon D. E., 2011, ApJ, 728, 44
Woon D. E., Dunning Thom H. J., 1993, J. Chem. Phys., 98, 1358
Yamato Y., Notsu S., Aikawa Y., Okoda Y., Nomura H., Sakai N., 2024, AJ, 167, 66
Yang Y.-L. et al., 2021, ApJ, 910, 20

APPENDIX A: PRUNING PROCEDURE

During the geometry optimization, multiple initial configurations of CH_3OH can converge to the same minimum on the potential energy surface (PES). This convergence is primarily due to the inherent complexity of the PES, the relatively weak interaction energies, and the extensive number of starting geometries considered. Tinacci et al. (2023) illustrated the importance of trimming redundant structures and proposed that RMSD and the ΔBE computed at the density functional theory (DFT) level serve as robust criteria for identifying structurally similar configurations. Given the considerable computational cost of calculating 486 BE sites at the DFT level, Bariosco et al. (2024) proposed applying the same pruning criteria to results obtained at the GFN2 level, demonstrating that comparable accuracy in structure pruning can be achieved. The criteria for the pruning procedure were established by correlating the RMSD and the absolute energy difference, $|\Delta E_{Cij}|$, for each possible pairing among model zones with an identical number of atoms. The left panel of Fig. A1 displays the correlation plot between RMSD and $|\Delta E_{Cij}|$ for all these combinations. The green rectangle is zoomed and plotted in the right panel of Fig. A1. As shown in the right panel of Fig. A1, a distinct cluster of points is evident in the lower left area, corresponding to redundant BE sites. Specifically, the orange rectangular region includes 263 redundant structures, which once removed results in a refined distribution comprising 223 BE sites.

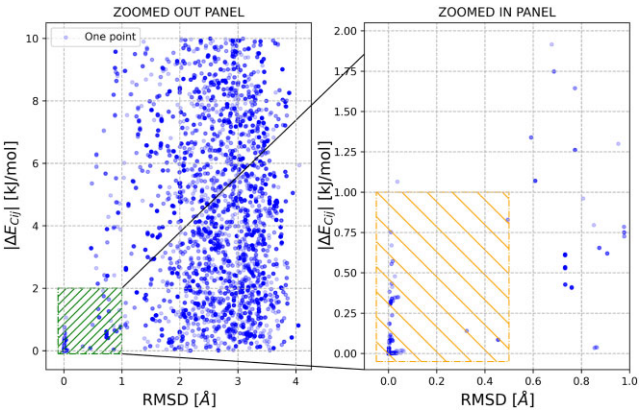

Figure A1. Correlation plot between $|\Delta E_{Cij}|$ and RMSD for CH_3OH binding sites at GFN2 level. In the left panel, the total scattered plot is reported. The dashed area is then zoomed and reported in the right panel. The rectangle in the right panel highlights the structures that the pruning procedure has identified as redundant. Transparency was set for each point to show data clustering.

APPENDIX B: BINDING ENERGY FORMALISM ADOPTED

The equation adopted for the calculation of the ONIOM BEs are:

$$\mathrm{BE}^{*} = -\Delta E = E^{\mathrm{iso}}_{\mathrm{ads}}(\mathrm{QM}) + E^{\mathrm{iso}}_{\mathrm{grn}}(\mathrm{QM{:}SQM}) - E_{\mathrm{c}}(\mathrm{QM{:}SQM}) \quad \text{(B1)}$$

where BE^{*} is the binding energy not corrected for the ZPE correction. BE∗ can be decomposed in the pure electronic interaction ($\mathrm{BE_e}$) corrected for the BSSE and the deformation energy (δE_{def}) contributions. The $\mathrm{BE_e}$ is given by:

$$\mathrm{BE_e} = E^{\mathrm{iso//c}}_{\mathrm{ads}}\big(\mathrm{G(grn)}\big) + E^{\mathrm{iso//c}}_{\mathrm{grn}}\big(\mathrm{G(ads)}\big) - E_{\mathrm{c}}(\mathrm{QM}) \,, \quad \text{(B2)}$$

where $E^{\mathrm{iso//c}}_{\mathrm{ads}}\big(\mathrm{G(grn)}\big)$ and $E^{\mathrm{iso//c}}_{\mathrm{grn}}\big(\mathrm{G(ads)}\big)$ are the energies of the isolated adsorbate and the grain in the geometries assumed in the complex ($iso//c$) in presence of the ghost orbitals of the grain G(grn) and the adsorbate G(ads), respectively. As the BSSE is already taken into account in the GFN2 method, equation (B2) only applies to the QM methods (*vide infra*) on the Model zone. The δE_{def} is defined:

$$\delta E_{\mathrm{def}} = \underbrace{\left(E^{\mathrm{iso//c}}_{\mathrm{ads}} - E^{\mathrm{iso}}_{\mathrm{ads}}\right)}_{\delta E^{\mathrm{ads}}_{\mathrm{def}}} + \underbrace{\left(E^{\mathrm{iso//c}}_{\mathrm{grn}} - E^{\mathrm{iso}}_{\mathrm{grn}}\right)}_{\delta E^{\mathrm{grn}}_{\mathrm{def}}} \,, \quad \text{(B3)}$$

where $\delta E^{\rm ads}_{\rm def}$ and $\delta E^{\rm grn}_{\rm def}$ are the deformation energy of the adsorbate and the surface, respectively. Vibrational frequencies were computed on the Model zone to obtain the ZPE correction, from which the ΔZPE resulted as:

$$\Delta\mathrm{ZPE} = \mathrm{ZPE_c} - \mathrm{ZPE^{iso}_{ads}} - \mathrm{ZPE^{iso}_{grn}} \ . \tag{B4}$$

Including all the above-mentioned contributions, equation (B1) becomes:

$$\mathrm{BE} = \underbrace{\mathrm{BE_e} - \left(\delta E^{\rm grn}_{\rm def} + \delta E^{\rm ads}_{\rm def}\right)}_{\mathrm{BE^*}} - \Delta\mathrm{ZPE} \ . \tag{B5}$$

This paper has been typeset from a TEX/LATEX file prepared by the author.